NAVAL ARCHITECTURE AND MARINE ENGINEERING
UNIVERSITY of MICHIGAN ■ COLLEGE of ENGINEERING

URANS Predictions of Resistance and Motions of the KCS in Head Waves

Grzegorz P. Filip, Wenzhe Xu, Kevin J. Maki

The University of Michigan
Department of Naval Architecture & Marine Engineering
Ann Arbor, Michigan, USA
gfilip@umich.edu, wenzhe@umich.edu, kjmaki@umich.edu

Technical Report Number 355
March 8, 2017

Abstract

This paper presents a computational-fluid-dynamics framework that is focused on the prediction of resistance and motions in waves. In particular, the framework is developed to predict the performance during operation in an extreme irregular seaway. A wave-focusing technique is presented that allows for the investigation of extreme dynamical events such as heave, pitch, or water-on-deck. The body motion is solved with an unique algorithm for the six rigid-body degrees-of-freedom. Waves are generated with the `waves2Foam` toolbox. The solver is validated for the case of a freely heaving cylinder, the propagation of regular waves, and the added resistance and motions of the KRISO container ship (KCS) in regular and irregular waves. Results are presented for an encounter of the KCS in an extreme heave event.

Keywords: Computational fluid dynamics, ship design, marine hydrodynamics, seakeeping

Contents

1 Introduction

The real seaway is composed of conditions ranging from quiescent through rough seas and strong winds that can limit the allowable operating conditions defined within the ship's safe operating envelope (SOE). The cost of operating the vessel is also affected by the increased resistance in waves and the increase in fuel consumption due to the potentially longer routes necessary to avoid the regions with dangerous sea conditions that are outside of the SOE. More recently, regulatory initiatives such as the Ship Energy Efficiency Operational Indicator (EEOI) originated by the International Maritime Organization (IMO) place an emphasis on the need for improvements in seakeeping performance in order to reduce the greenhouse gas emissions produced by the shipping industry. All these factors are a strong incentive to research and improve the operating performance of ships in waves.

1.1 Previous Work

The use of viscous flow solvers to study the seakeeping problem is challenging because of the need to accurately resolve the ambient and ship-generated wave fields in the time domain. The Wigley hull was an early hullform to be evaluated using CFD against the experimental measurements of [16] who studied the heave and pitch diffraction and radiation problems as well as the seakeeping performance in regular-head waves. [26] and [33] conducted seakeeping simulations based on a surface-tracking approach where the grid was adopted to the instantaneous free surface. This method was found to be limited to relatively small amplitude waves and body motions. More recently, interface-capturing methods such as the volume-of-fluid (VOF) and level-set methods have become the standard approach due to the their robustness across a wide range of conditions including extreme sea states.

The Workshops on CFD in Ship Hydrodynamics including the 2010 and the 2015 editions (see [18] and [19]) include seakeeping test cases based on several contemporary hull forms including an oil tanker, a container ship, and a Navy combatant. The workshops demonstrate an increased interest in using the viscous numerical solvers in seakeeping prediction due to the combined effect of the limitations of the reduced-order methods like potential-flow solvers and the reduced cost of CFD simulations as the high-performance computing (HPC) clusters become more accessible. The workshops use experimental data such as those of [29] to conduct code-to-code comparison and comparison against measured results from model tests where available. In the 2010 edition of the workshop, [6] and [21] both evaluated the KRISO container ship (KCS) hull form and reported good agreement with the experimental ship motions but more significant differences in the predicted added resistance. [6] conducted a comparison of the CFD codes Comet and OpenFOAM and found both to agree in the heave and pitch pre-

dictions. [21] utilized the code FreSCo+ to perform the same seakeeping analysis in regular head waves and found the added resistance coefficient to compare well against the experiments in several conditions but the amplitude of the resistance signal was mostly under predicted. [30] used two CFD solvers in the form of Star-CCM+ and CFDShip-Iowa as well as a potential flow solver *Aegir* to study the seakeeping problem. The viscous solvers were found to under predict the first harmonic of the total resistance by 50% to 90% but to outperform the potential-flow approach. [11] reported on the seakeeping analysis of the KVLCC2 tanker geometry using the unsteady RANS CFD solver ISIS-CFD. The CFD approach was recommended over simplified methods such as strip theory for sufficiently short wavelengths due to the improved added resistance prediction. The authors of [11] also recommend that the vessel be kept fixed in seakeeping analysis for wavelengths less than $0.63L_{PP}$ to improve the accuracy of the added resistance prediction. [28] and [34] also used CFD-based tools to evaluate the seakeeping characteristics of the KVLCC2 geometry in regular head waves. The numerical simulations were conducted using the code CFDShip-Iowa v4.5 which utilized the overset grid approach to facilitate the ship pitch and heave motion relative to the background grid. The added resistance trends were generally well predicted and found to increase with the increase in the relative bow motion but the first harmonic of the surge force was under predicted by an average of 35% across the tested wave lengths for the lowest Froude number.

Viscous flow solvers have also been applied to multi-hull geometries such as the DELFT 372 catamaran studied by [5] using CFDShip-Iowa. The investigators found the RANS approach to yield more accurate ship motion predictions outside of the resonant conditions when compared against the strip-theory approach. [20] studied a concept design of an adjustable-length trimaran using an extensive series of physical experiments, a viscous flow slower FLUENT, a thin-ship theory approach, and the classical strip theory. Furthermore, CFD tools have also been used to perform full-scale resistance and seakeeping analysis with emphasis on improving the ship's performance when slow-steaming as demonstrated by [9] and [32].

1.2 Current Work

The current work focuses on the development and validation of a viscous flow solver constructed upon the open-source CFD toolkit OpenFOAM. The specific focus of the custom solver is to predict the seakeeping performance, both motions and resistance, of ships in a wide range of conditions. To validate the solver numerical simulations are shown for the calm-water resistance prediction and a series of regular head-wave resistance calculations for the model-scale KCS hull-form. Finally, the validated solver is used to compute the operation of the KCS in an extreme event that occurs in an irregular seaway. The paper is organized as follows. First, the principle elements of the numerical flow solver are pre-

sented. Specifically the flow solver and the body-equation-of-motion technique are described and evaluated on a validation problem of a freely heaving cylinder. Then, the wave-generation process is described and the accuracy is assessed for the problem of the propagation of regular waves. Finally the main results section summarizes the added resistance study for the container ship in regular and extreme irregular waves.

2 Numerical Method

The computational toolkit is based on the open-source CFD platform OpenFOAM. The customized toolkit uses the finite-volume cell-centered discretization applied on arbitrary grid topologies as discussed by [15]. The discretized governing equations that govern the fully nonlinear viscous-fluid flow can treat important phenomena such as wave breaking, etc., as demonstrated by [7]. The air-water interface is captured using the volume-of-fluid (VOF) approach of [12] and the surface tension is represented using the continuum surface force method of [4]. Wave generation is achieved using the `waves2Foam` extension presented in [14].

2.1 Governing Equations

The Reynolds-averaged incompressible Navier-Stokes equations are given by:

$$\nabla \cdot \mathbf{u} = 0, \tag{2.1}$$

$$\frac{\partial \rho \mathbf{u}}{\partial t} + \nabla \cdot \rho \mathbf{u}\mathbf{u} = -\nabla p - \mathbf{g} \cdot \mathbf{x} \nabla \rho + \nabla \cdot \left[\mu_{\text{eff}} \left(\nabla \mathbf{u} + \nabla \mathbf{u}^T \right) \right] \tag{2.2}$$

where $\mathbf{u}$ is the fluid velocity, ρ is the fluid density, $\mu_{\text{eff}} = \mu + \mu_t$ is the effective dynamic viscosity, $\mathbf{g}$ is the gravity vector, and p is the dynamic pressure. The turbulent viscosity μ_t is a function of the turbulence model. The velocity vector is expressed in the earth-fixed inertial coordinate system. This allows for easy specification of the free-stream conditions for the fluid velocity and the ambient waves. Thus the ship moves relative to this coordinate, and the equations are solved using the arbitrary-Eulerian-Lagrangian (ALE) method that has the convective term use the relative velocity flux. The pressure is solved using a PISO-like algorithm.

The VOF equation combined with the artificial compressive velocity $\mathbf{w}$ is solved to advect the volume fraction α and to maintain a sharp fluid interface:

$$\frac{\partial \alpha}{\partial t} + \nabla \cdot \mathbf{u}\alpha + \nabla \cdot \mathbf{w}(\alpha(1-\alpha)) = 0. \tag{2.3}$$

Additional details about the compressive velocity field construction can be found in [3, 24, 27]. The air-water flow is represented using the one-fluid formulation where the VOF variable is used to keep track of the two phases within the domain:

$$\rho(\mathbf{x},t) = \rho_w \alpha(\mathbf{x},t) + \rho_a (1 - \alpha(\mathbf{x},t)) \tag{2.4}$$

$$\mu(\mathbf{x},t) = \mu_w \alpha(\mathbf{x},t) + \mu_a(1-\alpha(\mathbf{x},t)). \tag{2.5}$$

The subscripts w and a represent water and air, respectively.

In the adopted URANS approach, the turbulent viscosity μ_t models the Reynolds stresses based on the Boussinesq hypothesis. The two-equation $k-\omega$ *SST* model of [23] is used to model the effects of turbulence because the model has been demonstrated to perform well for flows with adverse pressure gradients such as the flow in the stern area of a typical displacement hull. The model solves two transport equations for the turbulent kinetic energy k and its specific dissipation ω:

$$\frac{\partial k}{\partial t} + U_j \frac{\partial k}{\partial x_j} = P_k - \beta^\star k\omega + \frac{\partial}{\partial x_j}\left[(\nu + \sigma_k \nu_t)\frac{\partial k}{\partial x_j}\right] \tag{2.6}$$

$$\frac{\partial \omega}{\partial t} + U_j \frac{\partial \omega}{\partial x_j} = \alpha S^2 - \beta\omega^2 + \frac{\partial}{\partial x_j}\left[(\nu + \sigma_\omega \nu_t)\frac{\partial \omega}{\partial x_j}\right] + 2(1-F_1)\sigma_{\omega 2}\frac{1}{\omega}\frac{\partial k}{\partial x_i}\frac{\partial \omega}{\partial x_i} \tag{2.7}$$

where the eddy viscosity is defined as:

$$\nu_t = \frac{a_1 k}{max(a_1\omega, SF_2)}. \tag{2.8}$$

The constants and auxiliary closure terms are detailed in [23].

The discretized equations can be solved with a variety of numerical schemes and solvers available in the toolkit. In the present work, second-order spatial discretization schemes are used together with the first-order Euler implicit scheme for time integration. The divergence term is treated with a second-order linear upwind scheme to preserve numerical stability while retaining the nominal second-order accuracy. The diffusion term is discretized with a second-order central difference. The volume-fraction divergence term is discretized using the vanLeer scheme to maintain its boundedness. The VOF equation can be solved with either an implicit or an explicit discretization. With the explicit discretization the multidimensional universal limiter for explicit solution (MULES) method is used. For the implicit discretization the deferred-correction approach is used for the higher-order part of the discretization.

2.2 Rigid-Body Motion Solver

The fluid and rigid-body equations are advanced in time with a tightly-coupled algorithm. The fluid solution is influenced by the rigid-body response in the velocity boundary condition on the fluid-structure interface. The rigid-body solution is coupled to the fluid through the fluid stress distribution on the hull surface. In the first step of the time advancement, the body motion is updated using the most recent value of the force from the previous time step, and then the fluid equations are solved about the predicted position. This process is repeated multiple times at each time step to tightly couple the solutions at the new time level, in this way

the equations use the body motion and the fluid solution that together satisfy their governing equations at the new time step.

The solution of the rigid-body motion is governed by the following equation:

$$\mathbf{M}\ddot{\mathbf{q}} = \mathbf{f}(\ddot{\mathbf{q}}, \dot{\mathbf{q}}, \mathbf{q}) \tag{2.9}$$

where $\mathbf{M}$ is the mass matrix, $\mathbf{q}$ is the displacement vector, and $\mathbf{f}$ is the external force vector that contains the force due to gravity, the hydrodynamic and hydrostatic forces, and any external constraints such as springs and dampers that could be used to model the attachment of a ship model to a carriage. The force depends on the acceleration, velocity, and position. This functional dependence can also be thought of as the added mass, damping, and hydrostatic components of the fluid force on the body. The added mass is often of the same order of magnitude as the physical mass and can have a destabilizing effect on the numerical solution algorithm. In other words, the right-hand side of equation 2.9 is determined from the solution of the fluid governing equations, and so the technique to solve equation 2.9 appears to be explicit since the fluid force is solved in a separate step from the body equation of motion. At the completion of the iteration at each time step the solution for both the body and the fluid are both fully implicit, but during the iteration there is the possibility to not converge. This becomes particularly true for the case in which the fluid added mass is large relative to the rigid-body physical mass.

In order to stably solve for the body and structural motion, the governing equation is modified with an inertial under-relaxation technique as follows:

$$[\mathbf{M} + \blacksquare]\,\ddot{\mathbf{q}} = \mathbf{f} + \blacksquare\tilde{\ddot{\mathbf{q}}} \tag{2.10}$$

Here, $\blacksquare$ is a user-specified added-mass matrix used to under-relax the system and retain stability, and $\tilde{\ddot{\mathbf{q}}}$ is an estimate of the acceleration vector. This idea has been used in other fluid-structure-interaction algorithms, for example [31, 35]. Note that during the iteration over the equations of the body and fluid motion, the discretized form of the equation is solved several times and the estimate of the acceleration converges to the solved-for value, making the terms with the user-specified added mass matrix cancel each other so that the solution of equation 2.10 also satisfies the original equation of motion (equation 2.9). In other words if $\ddot{\mathbf{q}} = \tilde{\ddot{\mathbf{q}}}$, then $\mathbf{q}$ satisfies both equations 2.9 and 2.10. The iteration between the fluid and body equations is performed until this criterion is satisfied.

Analysis of the under-relaxation technique shows that a positive coefficient stabilizes the numerical solution and a larger value provides more stability. This is important in cases where the body mass is small relative to the fluid added mass. Tests on simple cases have shown that the user-specified added-mass can be chosen to be the same order as the physical mass [25]. In these cases three iterations over the entire equation set is sufficient for convergence.

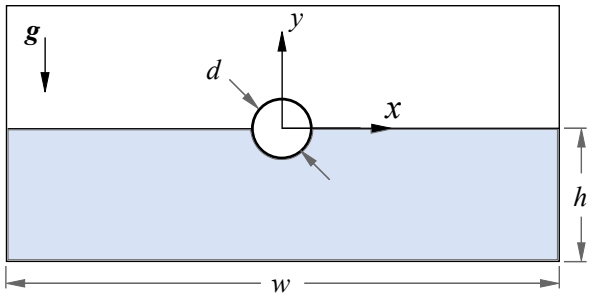

Figure 2.1: Sketch of the cylinder heave decay validation problem (extents not to scale)

2.2.1 Validation: Heave of a Freely Floating Cylinder

The rigid-body motion solver is validated by simulating the heave motion of a freely floating circular cylinder. The selected test case is a relatively simple problem but sufficient to elucidate stability and accuracy of the rigid-body motion solver. The combination of the fluid and the rigid-body motion solvers must accurately resolve the interaction of the waves generated by the oscillation of the cylinder and the associated forces acting on the body. The CFD results are compared against the experimental study of [13] and the theoretical solution of [22].

The sketch of the test problem is illustrated in Fig. 2.1. The domain size is based on the work of [10] where the cylinder diameter is $d = 0.1524$ m, the water depth is $h/d = 7.9$, and the domain has a total width of $w/d = 131$. The cylinder has a density of 500 kg/m^3. The coarse two-dimensional grid (G1) is built with 64 points around the cylinder perimeter and a total of 23,300 cells. A refined grid (G2) is built with 128 points around the perimeter and a total of 93,200 cells.

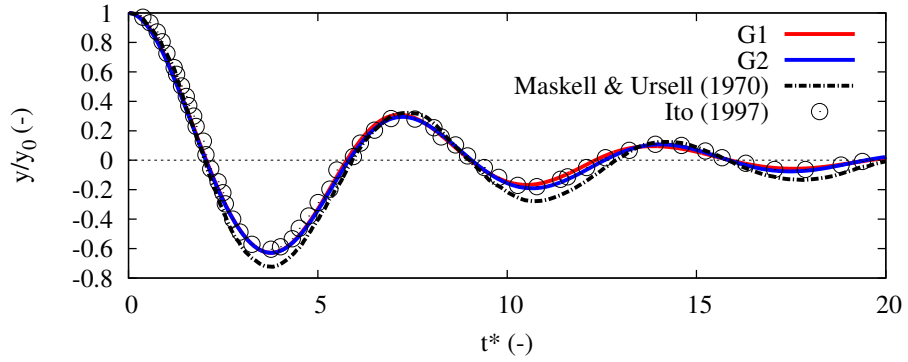

Figure 2.2: Heave oscillation of a freely floating cylinder with an initial displacement of $y_0 = d/6$.

The cylinder is given an initial vertical displacement of $y_0 = d/6$ and zero velocity at $t = 0$ s. Upon release, the cylinder is free to oscillate in heave only and the generated waves transfer energy away from the cylinder and the motion

decays. Fig. 2.2 shows the heave motion as a function of non-dimensional time $t^* = t\sqrt{g/d}$. The theoretical solution of [22] is shown to result in larger negative amplitudes of the decay signal. The difference between the theoretical results and the other solutions is likely due to the neglect of viscosity in the theoretical solution. The two results from the present study closely match the experimental data points in both the amplitude of the motion and the period of oscillation. The solution is found to be converged based on the relatively small differences between the results computed on the coarser grid and the refined grid.

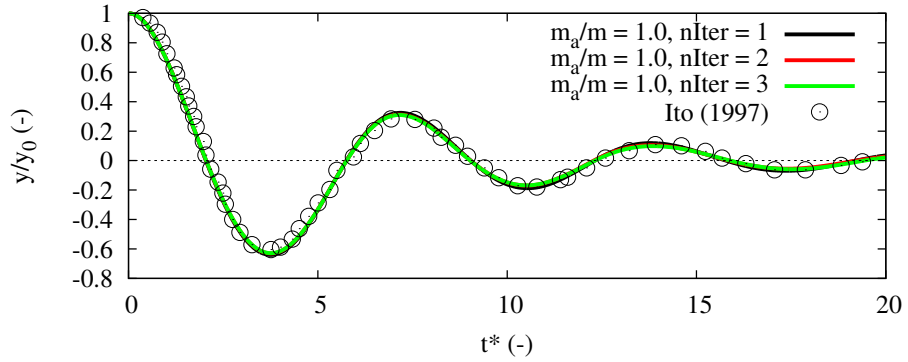

Figure 2.3: Convergence of the heave oscillation as a function of the number of solver iterations.

The convergence of the rigid-body motion solver as a function of the iteration number is also examined and summarized in Fig. 2.3. The estimated added mass is set equal to the physical mass of the cylinder and the solution is calculated on the refined grid G2 using one, two, and three rigid-body solver iterations. A small difference in the heave motion is observed when the solution is obtained with just one iteration. The solution is shown to be converged once two or more iterations are used.

2.3 Wave Generation

The wave generation utility `waves2Foam` originated by [14] is used to generate the ambient wave environment. The utility is based on the use of relaxation zones adjacent to the inlet and outlet boundaries where the waves are generated and absorbed, respectively. The target solution prescribed at the boundaries is computed based on the desired wave theory such as the Stokes' wave theory (of varying order, 1st, 2nd, 5th, etc.), stream function waves, cnoidal waves, etc. The water velocity and the volume fraction are prescribed within the relaxation zones using a spatially varying weighing factor $\chi(\sigma)$:

$$\phi = \chi(\sigma)\phi_{BC} + (1-\chi(\sigma))\phi_{\text{comp}} \tag{2.11}$$

where ϕ is the water velocity or the volume fraction. The relaxation weight is used to transition between the prescribed value of the variable of interest ϕ_{BC}, and the

solved-for value ϕ_{comp}, that is computed from the discretized governing equations. The weight factor takes the form:

$$\chi(\sigma) = 1 - \frac{\exp(\sigma^{\beta}) - 1}{\exp(1) - 1} \tag{2.12}$$

where σ is a local coordinate and β is the strength constant of the relaxation zone, here taken as the default value of $\beta = 3.5$.

The adopted wave-generation methodology is validated using a series of wave flume simulations in Section 3.

2.4 Wave Generation for Extreme Events using Design-Loads Generator (DLG)

The performance assessment of marine systems under extreme loads is critical to naval architects and marine engineers for purpose of developing a safe design. Unfortunately, since extreme events are stochastic processes, measurement or simulation requires long-exposure-time windows to observe highly rare events, this nature of extreme events renders the process of using experiments or nonlinear simulations expensive if not impossible since extremely long time windows must be investigated. The design-loads generator (DLG) uses information about the dynamical system and the operating environment to construct deterministic extreme events in the time domain. A wave-focusing technique is used to prescribe the wave environment with `waves2foam`.

The DLG has been under theoretical development since the work of [1, 2]. The basic underlying principle uses order statistics and dynamical system theory to focus waves that lead to an extreme dynamical response. More recently [17] further advanced the DLG theory by reducing the computational expense through the application of an acceptance-rejection algorithm to correct the assumptions of the processes to be independent and non-identically distributed.

The starting point of the DLG is the distribution on the largest sample of a process based on n samples.

$$f_{X_n}(x) = n f_X(x) \left(F_X(x)\right)^{n-1} \tag{2.13}$$

where X is any random variable, X_n is the largest among n samples, and $f_X(x)$ and $F_X(x)$ are probability-density function (PDF) and cumulative distribution function (CDF) respectively. The wave elevation and ship motion are assumed to be Gaussian random processes. Order-statistics theory gives the distribution of largest value (the extreme event). The DLG is used to find phases Θ_i for each frequency component to agree with this extreme value distribution $f_{X_n}(x)$:

$$X_n = \sum_{i=1}^{N} a_i \cos(\Theta_i) \tag{2.14}$$

where n is sample size depending on rareness of the events and N is the upper bound of the series. The amplitudes a_i are determined from the wave spectrum.

The phases are generated based on the modified Gaussian model. The extreme event samples from these phases turn out to be a distribution with similar mean but larger variance compared to the order statistics theory. Hence, acceptance-rejection algorithm is needed to filter out phase sets following the theory.

3 Wave Flume

3.1 Computational Grid and Wave Conditions

The wave-generation method is validated using a series of wave flume simulations to quantify the wave-propagation error associated with the numerical discretization.

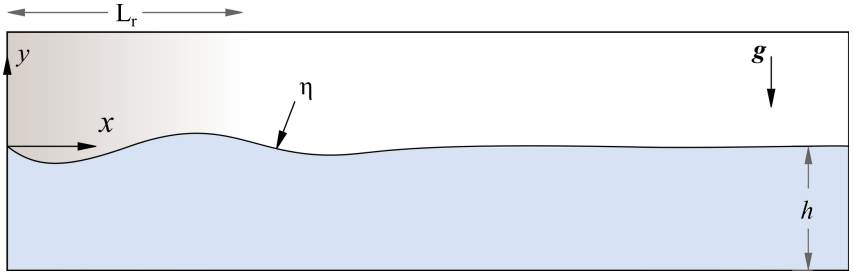

Figure 3.1: Sketch of the wave flume domain (extents not to scale)

The computational domain is a two-dimensional slice of the three-dimensional grid used for the KCS simulations to ensure a consistent comparison. A sketch of the domain is shown in Fig. 3.1. The waves are generated at the inlet boundary with a relaxation zone of length L_r that ends upstream of where the bow of the vessel is placed. The generated waves propagate through the domain and a series of wave probes is used to monitor the wave amplitude and phase. The wave conditions C1 through C5 are the same as those used in the ship seakeeping analysis in Section 4 (see Table 3.1). The wave conditions C6-C10 have the same wave length and period as C1-C5 but the wave amplitude is doubled to increase the wave steepness by a factor of two. The water depth h is 15 m and the waves propagate in the positive x direction.

Table 3.1: Wave conditions for the wave flume validation

Case	C1	C2	C3	C4	C5	C6	C7	C8	C9	C10
Wavelength: λ (m)	3.949	5.164	6.979	8.321	11.840	3.949	5.164	6.979	8.321	11.840
Wave height: H (m)	0.062	0.078	0.123	0.149	0.196	0.124	0.156	0.246	0.298	0.392
Wave steepness: $k\zeta$	0.051	0.047	0.055	0.056	0.052	0.102	0.094	0.110	0.112	0.104
Wave period: T (s)	1.590	1.819	2.114	2.309	2.753	1.590	1.819	2.114	2.309	2.753

3.2 Results

The error in the propagation of waves is computed as the root-mean-square (RMS) of the wave elevation signal at two different locations along the length of the domain. The difference between the computed instantaneous wave elevation η and the analytical wave elevation η_0 is used to compute the RMS using:

$$\eta_{\text{RMS}} = \sqrt{\frac{1}{n}\sum(\eta_n - \eta_{0,n})^2}. \tag{3.1}$$

The location of probe P1 corresponds to the bow of the KCS and probe P2 is placed $0.2L_{PP}$ downstream from the bow. The diffusive error computed for both wave-steepness ratios using two grid resolutions is shown in Fig. 3.2. Grid G1 is refined by a factor of two to generate grid G2. The error is normalized by the wave height H and plotted against the wave resolution parameter H/dz where dz is the nominal grid spacing in the proximity of the wave probes.

4 KRISO Container Ship

The first part of this section discusses the seakeeping characteristics of the KRISO container ship (KCS) model evaluated in regular head seas and compared against the experimental measurements presented by [29]. The regular head-seas experiments conducted by FORCE make up the validation case 2.10 in the 2015 Tokyo CFD Workshop. The present work includes the results submitted to the workshop as summarized in [8]. The second part of this section uses the response-amplitude operators predicted by the regular seas runs to perform a design event analysis of extreme heave in irregular seas.

4.1 Geometry and Regular-Wave Conditions

The KCS geometry was originated circa 1997 by the Korea Research Institute for Ships and Ocean Engineering (KRISO) in an effort to provide a set of experimental results for a realistic bulbous-bow container ship. The experimental data has been used extensively to evaluate various numerical simulation tools including CFD (see for example [18]). The hull form including the rudder and a wave deflecting block used in the FORCE experiments is shown in Fig. 4.1. The triangular block was used to minimize the occurrence of green water washing over the top of the model.

The main particulars of the FORCE model are give in Table 4.1. The captive model was towed at 2.017 m/s to achieve the design Froude number of 0.261 with a corresponding model-scale Reynolds number of 1.074×10^7. The model was free to heave and pitch with all other degrees-of-freedom fixed.

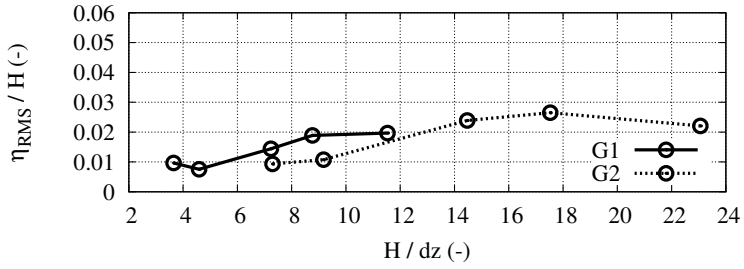

(a) $k\zeta \approx 0.05$, probe 1

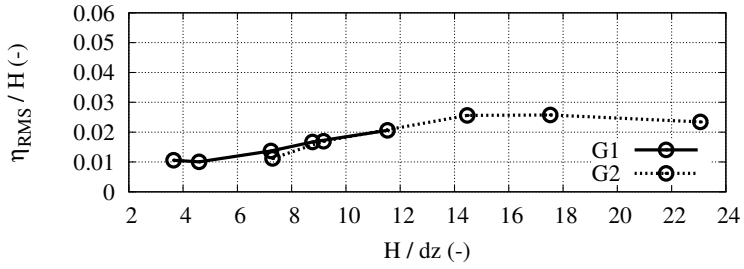

(b) $k\zeta \approx 0.05$, probe 2

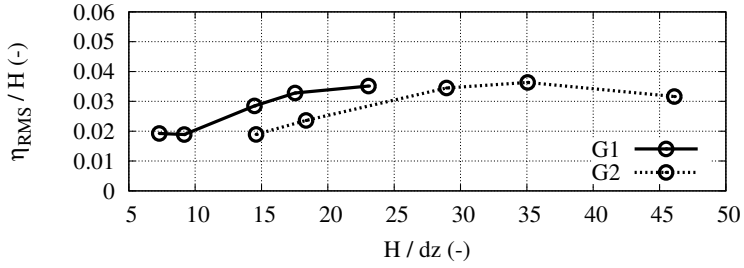

(c) $k\zeta \approx 0.10$, probe 1

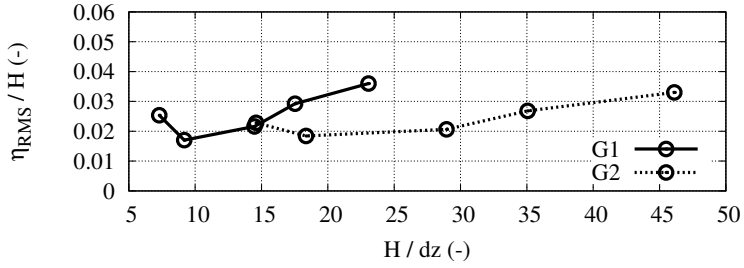

(d) $k\zeta \approx 0.10$, probe 2

Figure 3.2: Wave elevation RMS for the wave flume analysis

The experimental dataset is comprised of five regular wave runs in head seas (C1-C5), and a calm-water resistance run (C0). The wave conditions are summarized in Table 4.2. In the present work, the regular waves are generated using Stokes' fifth-order wave theory. The simulation length varies between 15 and 23 wave encounters for the shortest (C1) and longest (C5) wave conditions, respectively. The symbols ζ, $k = 2\pi/\lambda$, and λ are the wave amplitude, wave number,

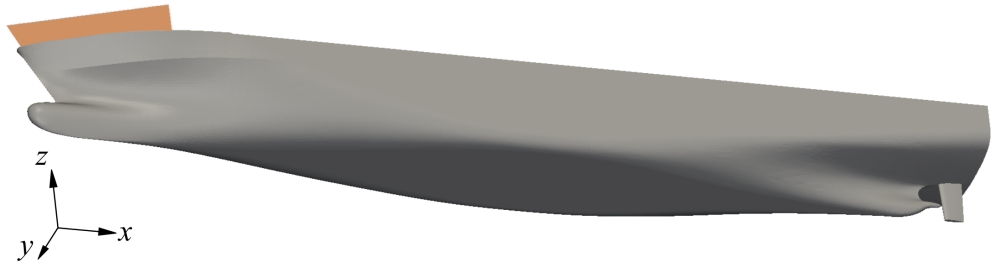

Figure 4.1: KRISO container ship (KCS) hull form with a wave deflecting block (highlighted in orange) used in the experiments to minimize the occurrence of green water on deck.

Table 4.1: Parameters of the KCS model test case

Scale factor	37.89	U	2.017 m/s
L_{PP}	6.0702 m	Fr	0.261
B_{WL}	0.8498 m	Re	1.074×10^7
T	0.2850 m	ρ_w	999.63 kg/m^3
∇	0.9571 m^3	ν_w	1.14×10^{-6} m^2/s

and wavelength, respectively.

Table 4.2: Wave conditions for the KCS seakeeping case

Case	C1	C2	C3	C4	C5
Wavelength: λ (m)	3.949	5.164	6.979	8.321	11.840
Wave height: H (m)	0.062	0.078	0.123	0.149	0.196
Wave steepness: $k\zeta$	0.051	0.047	0.055	0.056	0.052
λ/L_{PP}	0.65	0.85	1.15	1.37	1.95

4.2 Computational Grid

A sketch of the computational domain and its extents are shown in Fig. 4.2. The grid is symmetric about the centerline and extends one ship-length upstream, four ship-lengths downstream, two ship-lengths laterally, and 1.7 ship-lengths vertically. The wave-generation zone spans from the upstream boundary to approximately 0.2 ship-lengths in front of the bow. This is the same relaxation zone that is used to generate the results in Section 3.

Three systemically refined numerical grids are generated using the semi-automated tool snappyHexMesh (see Fig. 4.3). The grid generator takes in a background grid, the desired triangulated surface geometry, and a set of grid refinement parameters

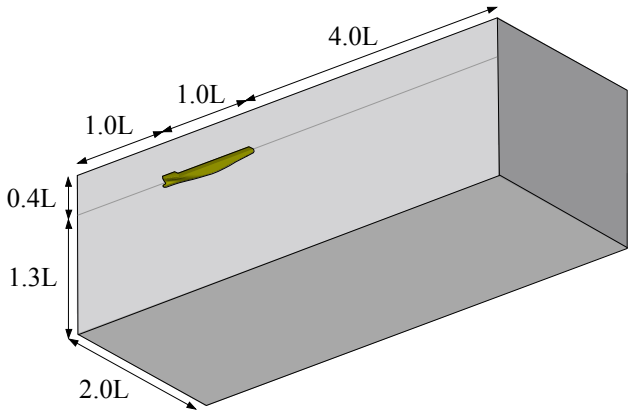

Figure 4.2: Details of the KCS computational domain

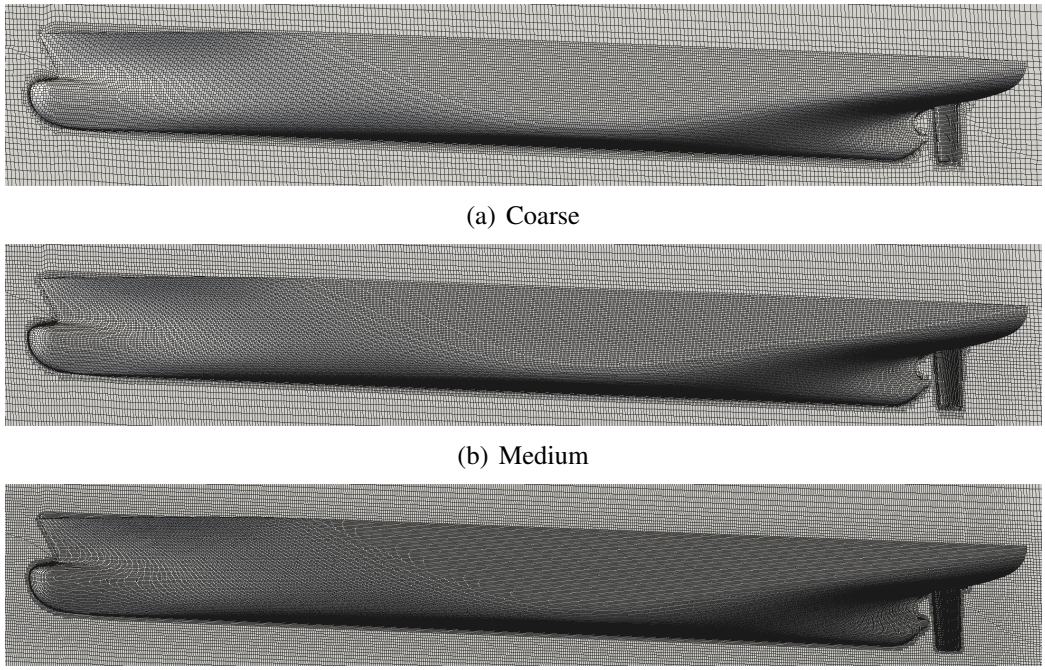

(a) Coarse

(b) Medium

(c) Fine

Figure 4.3: KCS hull grid refinement

to create the simulation-ready grid. The generation process can be performed in parallel and no user input is necessary beyond the initial setup used to specify any desired local refinements, the number of prism boundary layers, etc.

The resolution of the coarse, medium, and fine grids is selected so that the wave in the shortest wavelength case, C1, is resolved with 150, 220, and 300 cells per wavelength. The resultant grids are composed of 1.4 million, 3.8 million, and 10.1 million cells, respectively. The grid refinement study is conducted for the calm-water C0 condition to isolate the skin friction prediction from the influence

of the waves. The results of the grid refinement study are summarized in Table 4.3. The total resistance coefficient C_T is computed as:

$$C_T = \frac{R_T}{1/2\rho U^2 S_0} \tag{4.1}$$

where the total hydrodynamic drag R_T is composed of the skin friction and the pressure drag and it is computed by a surface integral over the ship hull:

$$R_T = \int_S \mathbf{i} \cdot \left(-p\mathbf{n} + \mu(\nabla \mathbf{u} + \nabla \mathbf{u}^T) \cdot \mathbf{n}\right) dS. \tag{4.2}$$

The skin friction coefficient C_F is compared to the ITTC57 line commonly used for vessel frictional resistance estimation:

$$C_F = \frac{0.075}{[\log_{10}(Re_L) - 2]^2} \tag{4.3}$$

In all dimensionless force results the calm-water wetted surface area S_0 is used.

Table 4.3: KCS grid refinement results for the calm-water condition

	Coarse	Medium	Fine	EFD	ITTC57
$C_T \times 10^3$	3.806	3.758	3.702	3.835	-
C_T E%D	-0.76%	-2.01%	-3.47%	-	-
$C_F \times 10^3$	2.939	2.962	2.929	-	2.963
C_F E%D	-0.81%	-0.03%	-1.15%	-	-
$C_{PV} \times 10^3$	0.867	0.794	0.773	-	-

The medium grid is selected for the seakeeping analysis. The near-wall resolution for the selected grid results in an average y^+ of 60 on the hull and of 25 on the rudder. The predicted sinkage and trim values on the medium grid are compared to the experiments in Table 4.4. The steady-state sinkage z normalized by the length between perpendiculars differs by approximately 8% which corresponds to an absolute difference of approximately 1 mm between the simulation and the experiment. The 11% difference in trim θ represents an absolute difference of 0.017 degrees.

Table 4.4: Calm-water sinkage and trim simulation (C0) results

	CFD	EFD	E%D
z/L_{PP}	-1.904E-03	-2.074E-03	8.18%
θ (deg)	-0.1820	-0.1646	-10.58%

4.3 Seakeeping in Regular Waves

The seakeeping analysis consists of five head-wave simulations with varying wavelength and height combinations. All five wave conditions have an approximately steepness $k\zeta$ of 0.05 and the wavelength varies from 65% of the ship length up to approximately 200%. The model-scale vessel is accelerated from rest to 2.017 m/s using a quarter-cosine ramp and it is allowed to move in the pitch and heave degrees of freedom. Sample instantaneous free-surface elevation contours for the calm-water resistance and the five seakeeping runs are illustrated in Fig. 4.4. The

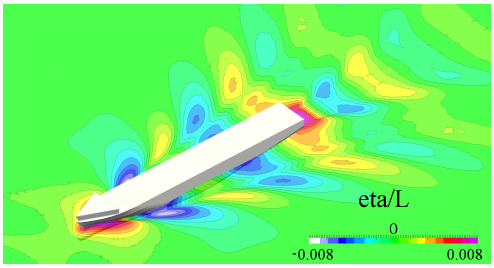

(a) C0: calm water

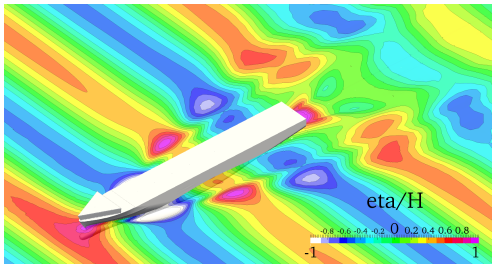

(b) C1: $\lambda/L_{PP} = 0.65$

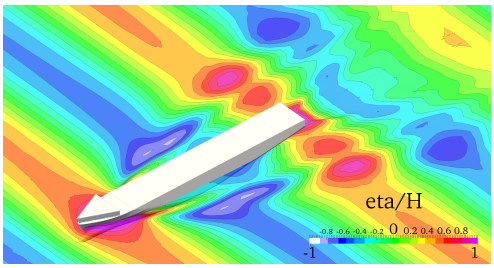

(c) C2: $\lambda/L_{PP} = 0.85$

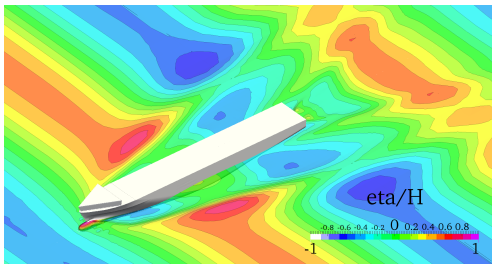

(d) C3: $\lambda/L_{PP} = 1.15$

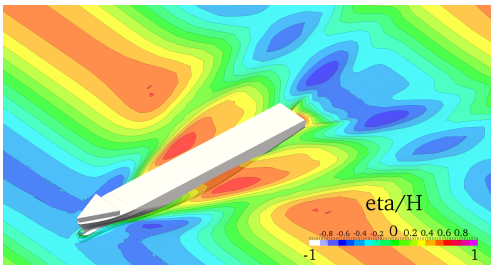

(e) C4: $\lambda/L_{PP} = 1.37$

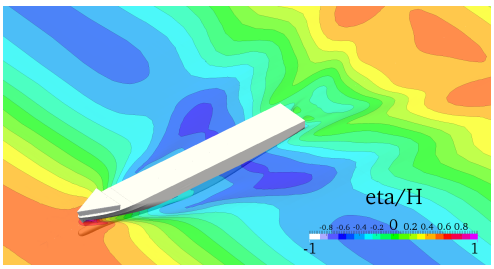

(f) C5: $\lambda/L_{PP} = 1.95$

Figure 4.4: Sample instantaneous free-surface elevations

interaction of the incoming waves and the ship-generated waves is shown to be strongly influenced by the ratio of the wavelength to the ship length.

The resistance and motion analysis is conducted based on a Fourier series reconstruction to extract the primary harmonics of the resultant signals. The re-

constructed time series $s_r(t)$ take the form:

$$s_r(t) = \frac{s_0}{2} + \sum_{n=1}^{N} s_n \cos(n\omega_e t + \gamma_n) \tag{4.4}$$

where s_n is the amplitude of the n-th harmonic and γ_n is the phase correction based on the the incident wave crest positioned at the forward perpendicular at $t = 0$ s. The mean value of the signal is the 0-th harmonic and the higher harmonics are computed using:

$$a_n = \frac{2}{T_e} \int_0^{T_e} s(t) \cos(n\omega_e t) dt \quad (n = 0, 1, 2, ...) \tag{4.5}$$

$$b_n = \frac{2}{T_e} \int_0^{T_e} s(t) \sin(n\omega_e t) dt \quad (n = 1, 2, 3, ...) \tag{4.6}$$

The corresponding amplitudes and the phase corrections are obtained from:

$$s_n = \sqrt{a_n^2 + b_n^2} \tag{4.7}$$

$$\gamma_n = \tan^{-1}\left(-\frac{b_n}{a_n}\right) \tag{4.8}$$

In the above analysis, ω_e is the wave-encounter frequency and T_e is the wave-encounter period. The same Fourier series reconstruction procedure is applied to the experimental signals.

A summary of the predicted and experimental mean seakeeping results is included in Table 4.5. The table includes the mean resistance coefficient C_T, mean heave z normalized by the wave amplitude ζ, mean pitch angle θ normalized by wave steepness ratio $k\zeta$, and the encountered wave amplitude normalized by the ship length-between-perpendiculars.

The mean resistance coefficient is found to be accurately predicted in all cases with the largest difference of 8.6% for the longest wavelength in case C5. The absolute difference for this case corresponds to approximately 11 N at model scale. The predicted resistance is within 4% for the three shortest wave conditions. The relative errors of the mean heave and pitch are larger than the resistance errors because their absolute value is significantly smaller. The mean heave is predicted to within 20% of the experiments where the largest discrepancy for case C4 is equal to approximately 4 mm for a model that is over six meters long. The largest difference in mean pitch is found in case C3 which was reported to suffer from resonance issues during the experimental campaign and thus the accuracy of the measured quantities may be compromised. Nonetheless, the absolute error between the CFD and the experiments is small across all test cases, including in the first harmonic results that are representative of the signal amplitude prediction. Table 4.6 compares the first harmonic results between the experiments and

Table 4.5: Mean results for the seakeeping runs in regular-head waves (C1 to C5)

$C_T \times 10^3$	C1	C2	C3	C4	C5
CFD	8.037	9.112	14.697	14.949	11.771
EFD	8.253	9.244	14.157	13.955	10.842
E%D	2.61%	1.43%	-3.82%	-7.13%	-8.57%
z/ζ					
CFD	-0.743	-0.549	-0.243	-0.201	-0.195
EFD	-0.809	-0.628	-0.278	-0.249	-0.201
E%D	8.11%	12.60%	12.65%	19.45%	2.67%
$\theta/k\zeta$					
CFD	-0.1197	-0.0994	-0.0014	-0.0042	-0.0568
EFD	-0.1078	-0.1303	-0.0026	-0.0069	-0.0562
E%D	-11.03%	23.70%	47.21%	39.42%	-1.06%
ζ/L_{PP}					
CFD	0.00509	0.00643	0.01010	0.01236	0.01602
EFD	0.00513	0.00641	0.01015	0.01230	0.01611
E%D	0.80%	-0.38%	0.51%	-0.45%	0.56%

Table 4.6: First harmonic results for the seakeeping runs in regular-head waves (C1 to C5)

$C_T \times 10^3$	C1	C2	C3	C4	C5
CFD	2.777	4.000	3.383	12.127	23.147
EFD	3.324	5.844	-	12.773	25.101
E%D	16.44%	31.56%	-	5.06%	7.79%
z/ζ					
CFD	0.1241	0.2285	0.9182	0.9236	0.9010
EFD	0.1286	0.2413	0.8993	0.8743	0.9312
E%D	3.48%	5.32%	-2.11%	-5.64%	3.25%
$\theta/k\zeta$					
CFD	0.0167	0.2302	0.7499	0.9984	1.0782
EFD	0.0163	0.1456	0.7483	0.9646	1.1185
E%D	-2.59%	-58.12%	-0.21%	-3.50%	3.61%

the simulations. The predicted heave and pitch amplitudes are within 6% of the experiments with the exception of pitch for case C2 with a difference of approximately 58% (this comparison is analyzed further in section 4.3.2). The resistance and ship motions are discussed in detail in the following sections.

4.3.1 Resistance in Waves

The resistance in waves is studied further by analyzing time histories of the reconstructed CFD and experimental data as well as the raw CFD resistance signal and its pressure and viscous components. The time histories shown in Fig. 4.5 span a single period of encounter for each seakeeping condition. The wave crest is at the forward perpendicular at $t/T_e = 0$.

The reconstructed signals compare well for all the considered cases. Only the constant mean value is plotted for C3 due to the resonance issues that were

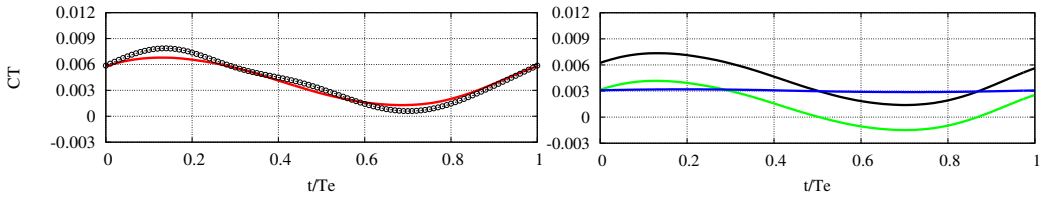

(a) C1: $\lambda = 3.949$ m, H = 0.062 m

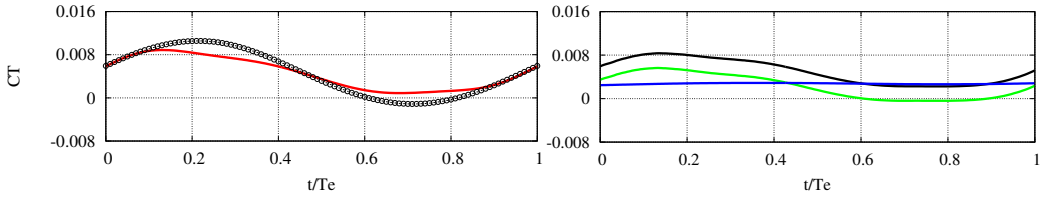

(b) C2: $\lambda = 5.164$ m, H = 0.078 m

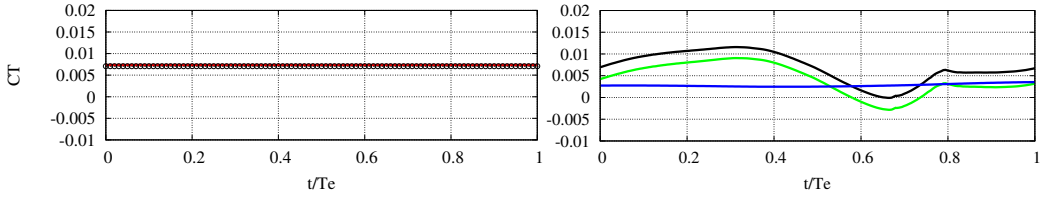

(c) C3: $\lambda = 6.979$ m, H = 0.123 m

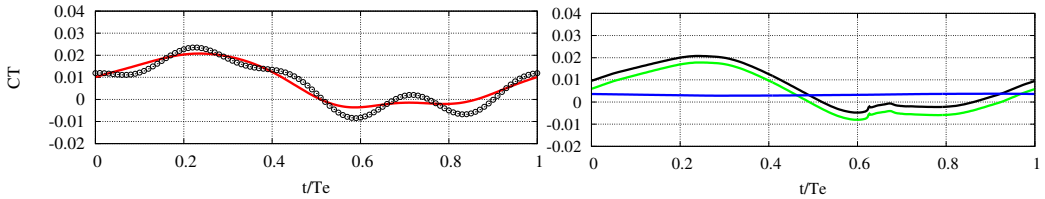

(d) C4: $\lambda = 8.321$ m, H = 0.149 m

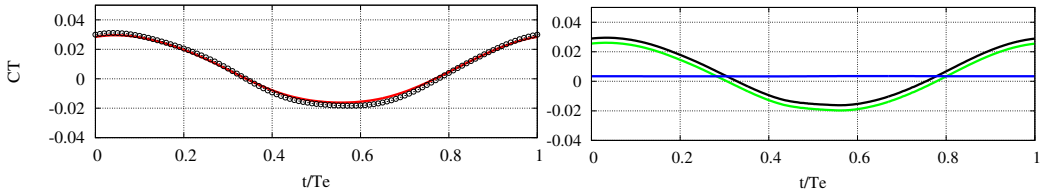

(e) C5: $\lambda = 11.840$ m, H = 0.196 m

Figure 4.5: Left columns: reconstructed resistance coefficient (solid red line) compared against experimental data (symbols). Right column: raw CFD resistance coefficient (black) and its pressure (green) and viscous (blue) components.

encountered during the experiments. For case C4, the high frequency content of the experimental signal is not fully captured by the Fourier reconstruction of the CFD data based on five coefficients. By using more coefficients the reconstruction is somewhat improved but not to the point of closely matching the experimental data. Fig. 4.6 shows the convergence of the reconstruction for cases C1 and C4 as a function of the number of Fourier coefficients. The reconstructed signal appears

to be fully converged with the use of ten or more Fourier coefficients for case C4, whereas two or more are sufficient for case C1. The oscillation observed in case C4 between approximately $t/T_e = 0.6$ and $t/T_e = 0.8$ is partially captured by the simulation but the earlier higher frequency content is not visible in the CFD signal. Furthermore, the maximum and minimum values are somewhat under predicted by the CFD. The lack of the higher frequency oscillation could be related to the shear stress predicted by the turbulence model.

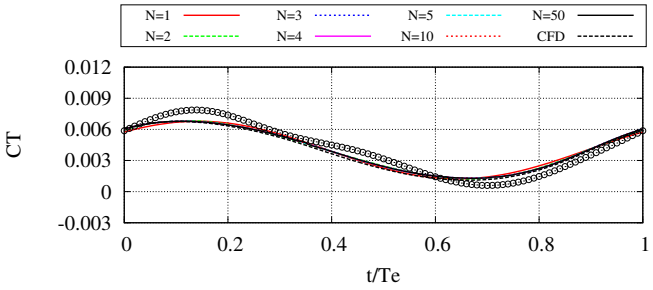

(a) C1

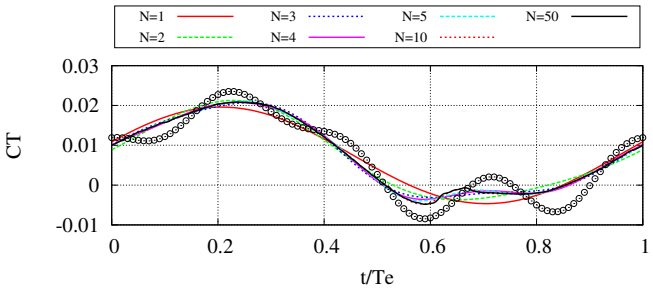

(b) C4

Figure 4.6: Resistance coefficient as a function of the number of Fourier coefficients (N) compared against experimental data (symbols)

The resistance signal peaks for the shortest wavelength cases C1 and C2 are under predicted. The peak and troughs of the reconstructed signals appear flattened especially for case C2. The difference is partially due to the limited number of Fourier coefficients used in present analysis. The shorter wavelengths used in these cases are also resolved with fewer cells per wavelength than the longer waves because the same grid resolution is used for all five conditions.

The zeroth (mean) and the first Fourier coefficient response amplitude operators (RAO) are plotted as a function of the wave-to-ship length ratio in Fig. 4.7. The under predicted maxima of the shortest wavelengths are illustrated by the amplitudes of the first harmonic. Cases C4 and C5, correspond to longer wavelengths and the CFD and the experimental data points match closely in the first harmonic comparison.

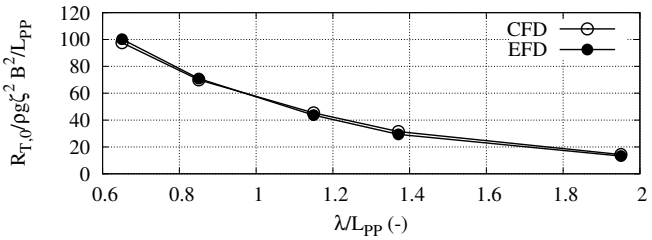

(a) Mean

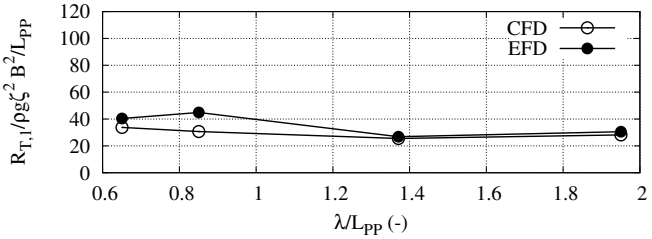

(b) First Harmonic

Figure 4.7: Total resistance in waves

4.3.2 Motion in Waves

The heave and pitch motion time series are shown in Fig. 4.8 and Fig. 4.9, respectively. The heave response closely replicates the experimental time series in all five seakeeping cases including the phase and the amplitude, especially for the longer wavelengths. The largest difference is found in the pitch response for case C2 where the CFD results over predict the amplitude by approximately 58%. Cases C1 and C2 correspond to the shorter wavelengths, and the heave and pitch RAO (shown in Fig. 4.10) indicate little motion. For example for C2 the heave and pitch RAO are both around 20%. The small excitation for the shorter wavelengths produce smaller motion and this makes the differences between the experiment and CFD larger.

The small differences in the simulated ship motions are summarized in Fig. 4.10 where the heave and pitch RAO's are shown. Overall, the adopted numerical method that combines URANS, wave generation, and the rigid-body motion solvers is demonstrated to accurately predict the seakeeping response of a realistic vessel advancing in regular head waves.

4.4 Seakeeping Response in Design Event

The DLG theory is used to generate a design event of extreme heave. A JONSWAP spectrum ($\gamma = 3.3$) with significant wave height $H_{1/3} = 0.132$ m and peak period $T_p = 2.01$ s is used to represent a seastate 6. The wave spectrum is shown in Fig. 4.11.

The DLG is used to generate a seaway that leads to an extreme heave motion

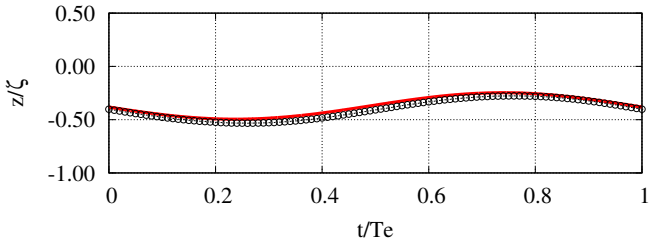

(a) C1: $\lambda = 3.949$ m, H = 0.062 m

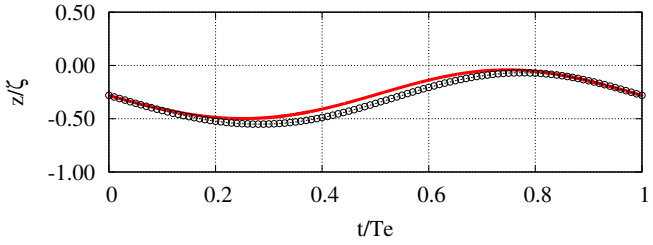

(b) C2: $\lambda = 5.164$ m, H = 0.078 m

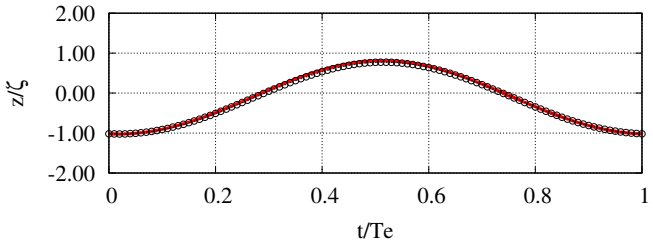

(c) C3: $\lambda = 6.979$ m, H = 0.123 m

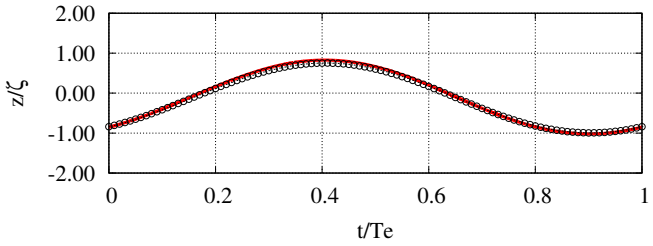

(d) C4: $\lambda = 8.321$ m, H = 0.149 m

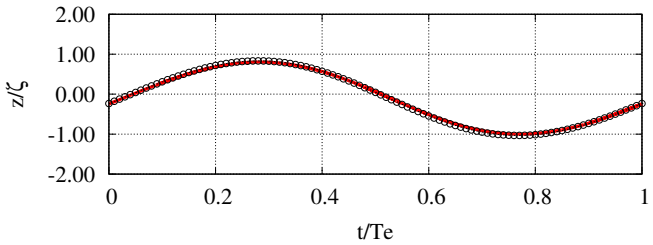

(e) C5: $\lambda = 11.840$ m, H = 0.196 m

Figure 4.8: Heave motion (solid line) compared against experimental data (symbols)

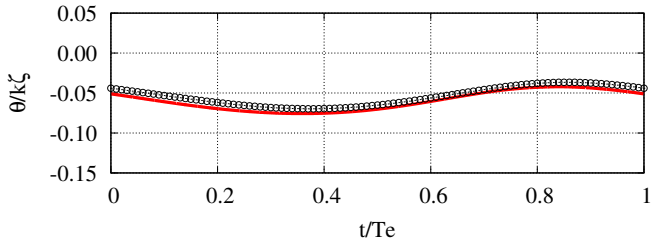

(a) C1: $\lambda = 3.949$ m, H = 0.062 m

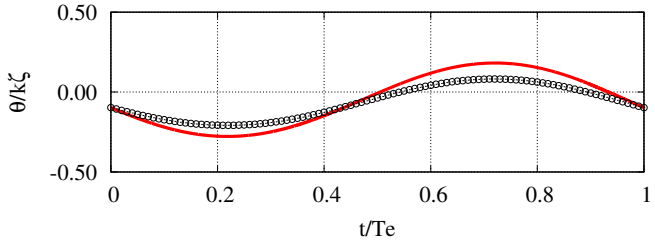

(b) C2: $\lambda = 5.164$ m, H = 0.078 m

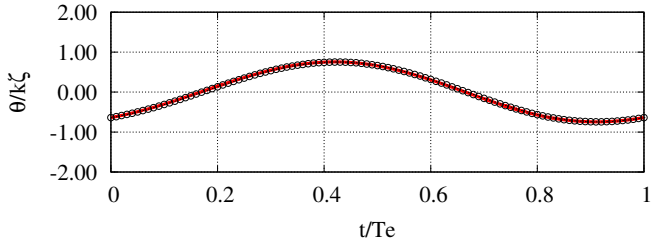

(c) C3: $\lambda = 6.979$ m, H = 0.123 m

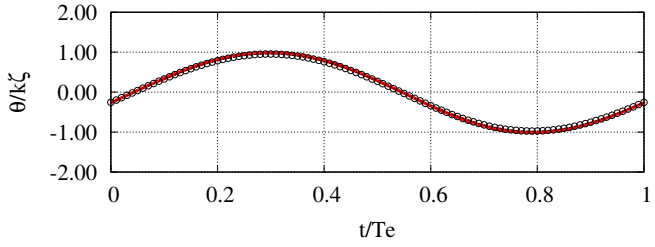

(d) C4: $\lambda = 8.321$ m, H = 0.149 m

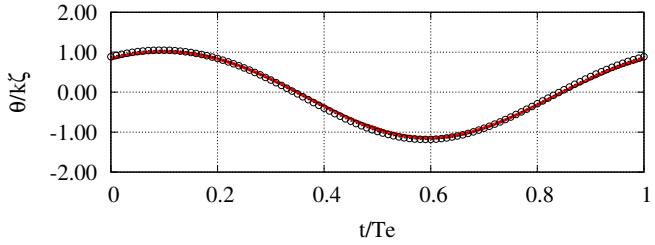

(e) C5: $\lambda = 11.840$ m, H = 0.196 m

Figure 4.9: Pitch motion (solid line) compared against experimental data (symbols)

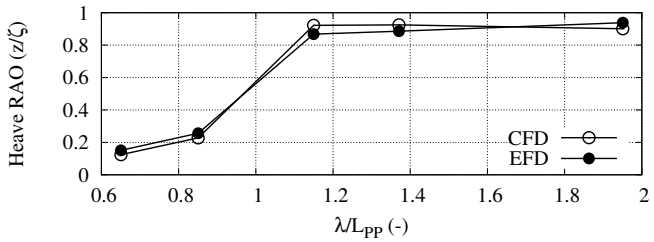

(a) Heave

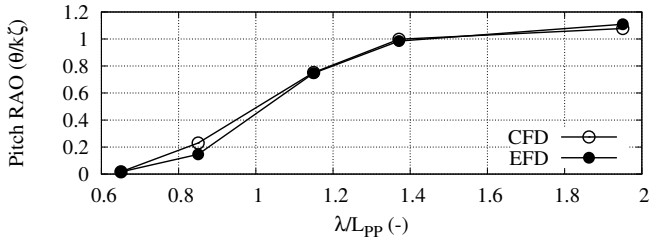

(b) Pitch

Figure 4.10: Pitch and heave RAO

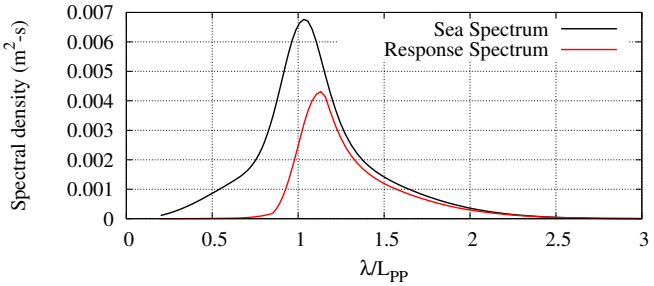

Figure 4.11: Input sea spectrum corresponding to SS6 at model scale and the response spectrum for the heave motion

in an exposure window of 17.6 hrs. This corresponds to a rareness of $\sigma = 4.0$. The relation between input wave spectrum and response spectrum is as follows:

$$S_o = |H(\omega)|^2 S_i \tag{4.9}$$

where $H(\omega)$ is the response amplitude operator (RAO) for corresponding vessel seakeeping analysis, and is taken from Fig. 4.10. The input spectrum yields the response spectrum scaled by the square of the linearly interpolated RAO. Fig. 4.11 also shows the response spectrum for heave motion.

The design event is selected to occur at 20 s (at model scale). The heave and pitch time series are shown in the top of Fig. 4.12, and the resistance coefficient is shown on the bottom. It is seen that the large heave (and pitch) excursion is seen around 22 s. The significant wave height is 13.2 cm, and the design wave encounter produces a wave that is 20.8 cm high. If linear theory is used to predict the extreme heave, the maximum is 5.4 cm whereas the nonlinear CFD prediction

shows the maximum heave of 6.8 cm. Thus the linear theory under-predicts the extreme value by approximately 20%. While linear theory is very useful for events that are correctly described by it, linear theory is difficult to use to accurately assess extreme events. Four time snapshots around the design event are illustrated in Fig. 4.13 to demonstrate the occurrence of green-water on deck and the extreme heave excursion where the bulbous bow exits the water.

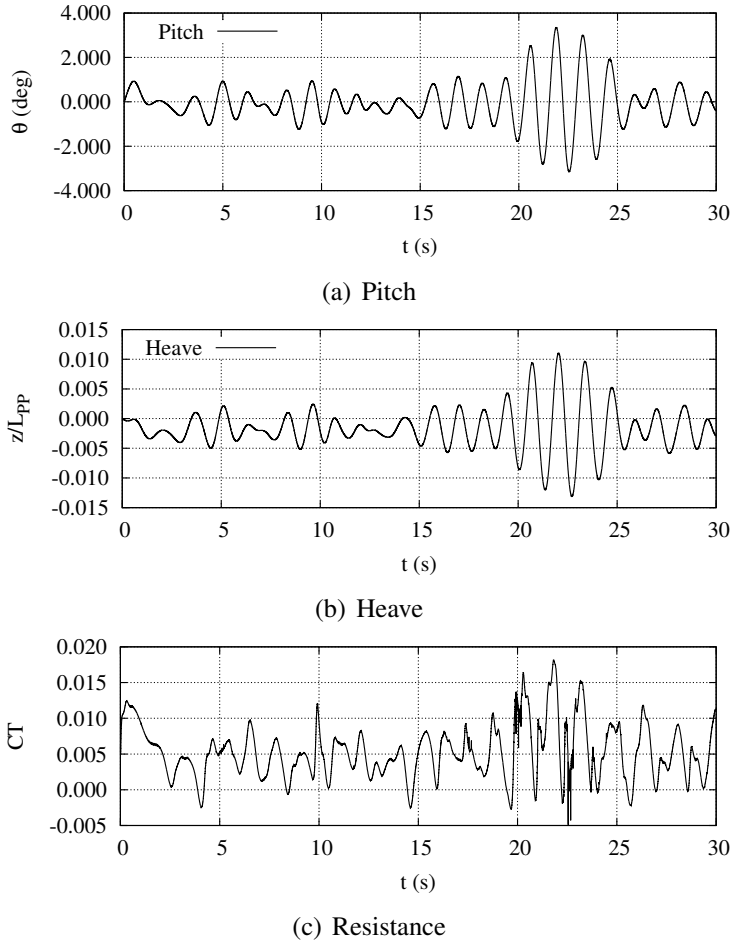

(a) Pitch

(b) Heave

(c) Resistance

Figure 4.12: DLG motions and resistance time histories

5 Conclusion

This paper presents a computational-fluid-dynamics framework for the prediction of ship motions and resistance in an extreme wave environment. A unique element of the solver is the method in which the body equations of motion and wave generation are included into the solver algorithm. Specifically, it is shown that the body equations of motion can be integrated in a stable manner for the simple problem

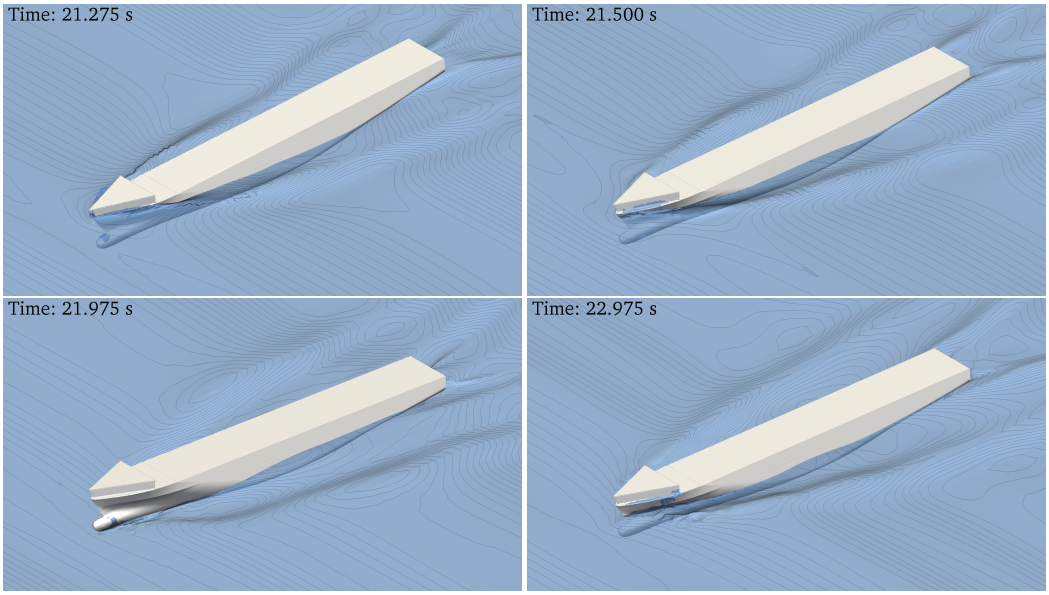

Figure 4.13: Sample time snapshots showing green-water on deck and large pitching motion shortly after the design event (t = 20 s)

of a vertically oscillating cylinder and the motions of the KRISO container ship (KCS) in head seas. The ambient waves are generated with the `waves2Foam` toolkit, and the fluid motion is taken to be governed by the URANS equations with the $k-\omega SST$ turbulence model.

The prediction of the forces and motions is shown to be in close agreement with the experimental measurements over a wide range of wave conditions. Finally, the solver is used to focus waves that lead to an extreme design event of large heave motion.

Acknowledgments

The authors are grateful for the support of the Office of Naval Research through grants N00014-13-1-0558 and N00014-14-1-0577 under the technical direction of Ms. Kelly Cooper. This research was supported in part through computational resources and services provided by Advanced Research Computing at the University of Michigan, Ann Arbor.

References

[1] Laura Alford, Dae-Hyun Kim, and Armin W. Troesch. Estimation of extreme slamming pressures using the non-uniform Fourier phase distributions

of a design loads generator. *Ocean Engineering*, 38(5-6):748–762, April 2011.

[2] Laura K. Alford and Armin W. Troesch. Generating extreme ship responses using non-uniform phase distributions. *Ocean Engineering*, 36:641–649, 2009.

[3] Edin Berberović, Nils P. van Hinsberg, Suad Jakirlić Ilia V. Roisman, and Cameron Tropea. Drop impact onto a liquid layer of finite thickness: Dynamics of the cavity evolution. *Physical Review E*, 79, 2009.

[4] J. U. Brackbill, D. B. Kothe, and C. Zemach. A continuum method for modeling surface tension. *Journal of Computational Physics*, 100:335–354, 1992.

[5] Teresa Castiglione, Frederick Stern, Sergio Bova, and Manivannan Kandasamy. Numerical investigation of the seakeeping behavior of a catamaran advancing in regular head waves. *Ocean Engineering*, 38:1806–1822, 2011.

[6] B. el Moctar, J. Kaufmann, J. Ley, J. Oberhagemann, V. Shigunov, and T. Zorn. Prediction of ship resistance and ship motions using RANSE. In *Gothenburg 2010: A Workshop on Numerical Ship Hydrodynamics, Volume II*, 2010.

[7] Grzegorz Filip. *High-Resolution Numerical Simulation of Turbulent Interfacial Marine Flows*. PhD thesis, University of Michigan, 2013.

[8] Grzegorz Filip and Kevin J. Maki. Seakeeping analysis of the KCS vessl in regular waves. In *Proceedings of Tokyo 2015: A Workshop on CFD in Ship Hydrodynamics, Volume II*, 2015.

[9] Grzegorz Filip, Dae-Hyun Kim, Sunil Sahu, Jan de Kat, and Kevin Maki. Bulbous bow retrofit of a containership using an open source computational fluid dynamics (CFD) toolbox. *SNAME Transactions*, 122:244–262, 2014.

[10] Amirmahdi Ghasemi, Ashish Pathak, and Mehdi Raessi. Computational simulation of the interactions between moving rigid bodies and incompressible two-fluid flows. *Computers and Fluids*, 94:1–13, 2014.

[11] B. J. Guo, S. Steen, and G. B. Deng. Seakeeping prediction of KVLCC2 in head waves with RANS. *Applied Ocean Research*, 35:56–67, 2012.

[12] C. Hirt and B. Nichols. Volume of fluid (VOF) - method for the dynamics of free boundaries. *Journal of Computational Physics*, 39:201–225, 1981.

[13] S. Ito. Study of the transiet heave oscillation of a floating cylinder. Master's thesis, Massachusetts Institute of Technology, 1977.

[14] Niels G. Jacobsen, David R. Fuhrman, and Jorgen Fredsoe. A wave generation toolbox for the open-source cfd library: Openfoam. *Int. J. Numer. Meth. Fluids*, 70(9):1073–1088, 2012.

[15] Hrvoje Jasak. *Error Analysis and Estimation for Finite Volume Method with Applications to Fluid Flow*. PhD thesis, Imperial College, University of London, 1996.

[16] J. M. J. Journee. Experiments and calculations on four wigley hullforms. Technical report, Delft University of Technology, Ship Hydrodynamic Laboratory, 1992.

[17] DH Kim. *Design loads generator: Estimation of extreme environmental loadings for ship and offshore applications*. PhD thesis, University of Michigan, 2012.

[18] Lars Larsson, Frederick Stern, and Michel Visonneau. CFD in ship hydrodynamics—results of the gothenburg 2010 workshop. In Luís Eça, Eugenio Oñate, Julio García-Espinosa, Trond Kvamsdal, and Pål Bergan, editors, *MARINE 2011, IV International Conference on Computational Methods in Marine Engineering*, volume 29 of *Computational Methods in Applied Sciences*, pages 237–259. Springer Netherlands, 2013. ISBN 978-94-007-6142-1. doi: 10.1007/978-94-007-6143-8_14. URL `http://dx.doi.org/10.1007/978-94-007-6143-8_14`.

[19] Lars Larsson, Frederick Stern, Michel Visonneau, Nobuyuki Hirata, Takanori Hino, and Jin Kim. Tokyo 2015: A workshop on CFD in ship hydrodynamics. In *Proceedings, Volume II*, 2015.

[20] K.J. Maki, L. J. Doctors, R.M. Scher, W.M. Wilson, S. H. Rhee, A.W. Troesch, and R.F. Beck. Conceptual design and hydrodynamic analysis of a high-speed sealift adjustable-length trimaran. *Transactions of SNAME*, 116: 16–39, 2008.

[21] M. Manzke and T. Rung. Resistance prediction and sea keeping analysis with FreSCo+. In *Gothenburg 2010: A Workshop on Numerical Ship Hydrodynamics, Volume II*, 2010.

[22] S. J. Maskell and F. Ursell. The transiet motion of a floating body. *Journal of Fluid Mechanics*, 44:303–313, 1970.

[23] F. R. Menter. Two-equation eddy-viscosity turbulence models for engineering applications. *AIAA Journal of Computational Physics*, 32:1598–1605, 1994.

[24] Bo T. Paulsen, H. Bredmose, H. B. Bingham, and N. G. Jacobsen. Forcing of a bottom-mounted circular cylinder by steep regular water waves at finite depth. *J. Fluid Mech*, 755:1–34, 14.

[25] Dominic J. Piro. *A Hydroelastic Method for the Analysis of Global Ship Response Due to Slamming Events*. PhD thesis, University of Michigan, 2013.

[26] S. H. Rhee and F. Stern. Unsteady RANS method for surface ship boundary layer and wake and wave field. *International Journal of Numerical Methods for Heat and Fluid Flow*, 37:445–478, 2001.

[27] Henrik Rusche. *Computational Fluid Dynamics of Dispersed Two-Phase Flows at High Phase Fractions*. PhD thesis, University of London, London, England, December 2002.

[28] Hamid Sadat-Hosseini, Ping-Chen Wu, Pablo M. Carrica, Ho Kim, Yasuyuki Toda, and Frederick Stern. CFD vertification and validation of added resistance and motions of KVLCC2 with fixed and free surge in short and long head waves. *Ocean Engineering*, 59:240–273, 2013.

[29] C. Simonsen, J. Otzen, and F. Stern. EFD and CFD for KCS heaving and pitching in regular head waves. In *Proceedings of the 27th Symposium on Naval Hydrodynamics*, 2008.

[30] Claus D. Simonsen, Janne F. Otzen, Soizic Joncquez, and Frederick Stern. EFD and CFD for KCS heaving and pitching in regular head waves. *Marine Science Technology*, 18:435–459, 2013.

[31] Hui Sun and Odd M. Faltinsen. Predictions of porpoising inception for planing vessels. *J. Mar. Sci. Technol.*, 16(3):270–282, May 2011.

[32] Tahsin Tezdogan, Yigit Kemal Demirel, Paula Kellett, Mahdi Khorasanchi, Atilla Incecik, and Osman Turan. Full-scale unsteady RANS CFD simulations of ship behaviour and performance in head seas due to slow steaming. *Ocean Engineering*, 97:186–206, 2015.

[33] Gabriel David Weymouth, Robert Vance Wilson, and Frederick Stern. RANS computational fluid dynamics predictions of pitch and heave ship motions in head seas. *Journal of Ship Research*, 49:80–97, 2005.

[34] Ping-Chen Wu. *A CFD Study on Added Resistance, Motions and Phase Averaged Wake Fields of Full Form Ship Model in Head Waves*. PhD thesis, Osaka University, 2013.

[35] Yin Lu Young, Eun Jung Chae, and Deniz Tolga Akcabay. Hybrid algorithm for modeling of fluid-structure interaction in incompressible, viscous flows. *Acta Mechanica Sinica*, 28(4):1030–1041, 2012.